

GLACIER MONITORING FROM ASTER IMAGERY: ACCURACY AND APPLICATIONS

A. Käab¹, C. Huggel¹, F. Paul¹, R. Wessels², B. Raup³, H. Kieffer² and J. Kargel²

- 1. Department of Geography, University of Zurich, Winterthurerstrasse 190, CH-8057 Zurich, Switzerland, phone: ++41 1 635 51 46, fax: ++41 1 635 68 48, kaeaeb@geo.unizh.ch, www.geo.unizh.ch/~kaeaeb*
- 2. U.S. Geological Survey, 2255 N. Gemini Drive, Flagstaff, AZ 86001, U.S.A., www.glims.org*
- 3. National Snow and Ice Data Center, University of Colorado, 449 UCB, Boulder, CO 80309-0449, U.S.A., www.nsidc.org*

ABSTRACT

The optical sensor ASTER (Advanced Spaceborne Thermal Emission and Reflection Radiometer) on board the Terra satellite offers new possibilities for worldwide glacier monitoring. In this paper, its capability and accuracy for selected glaciological applications are evaluated. (a) ASTER's along-track stereo sensor allows for photogrammetric DEM generation. Here, we apply PCI Geomatica Orthoengine for that purpose. A vertical DEM accuracy of approximately ± 60 m RMS was found for complex high-mountain topography with maximum errors of up to 500 m. For smoother terrain an accuracy of roughly 15 m can be expected. (b) Automatic glacier mapping using the ASTER bands 3 (15 m resolution) and 4 (30 m resolution) revealed no significant differences to corresponding work based on Landsat TM bands 4 and 5. (c) The flow field for Tasman glacier, New Zealand, was successfully derived from repeated ASTER orthoimages. The striking results suggest that ASTER data might help to include ice flow into global glacier monitoring from space. (d) Combining above approaches of exploiting ASTER data with GIS-models represents a valuable tool for integrated hazard assessments from space: the outburst flood from the moraine lake Dig Tsho, Khumbu Himal, of 1985 was reconstructed from an ASTER DEM with good agreement to the actual flood.

INTRODUCTION

Presently, the USGS-led project Global Land Ice Measurements from Space (GLIMS) aims at compiling a complete satellite-derived inventory of land ice masses on earth (1). For that purpose it mainly relies on optical data from Landsat ETM+ (Enhanced Thematic Mapper) and ASTER (Advanced Spaceborne Thermal Emission and Reflection Radiometer, on board the Terra satellite). While the application of Landsat data to glacier mapping and monitoring is widely evaluated (e.g. 2, 3, 4), little is known about the potential use of ASTER imagery for that purpose. It is, therefore, the objective of this study to evaluate the benefit from ASTER data for glacier studies by accuracy assessments and application studies:

- (a) an automatic DEM from ASTER data is compared to one derived from aerial photogrammetry. Such DEMs are of crucial importance for the accurate ortho-projection of ASTER imagery which is necessary for overlay of repeated imagery and other geo-information. In addition, ASTER-DEMs allow for geomorphometric modelling which is able to supplement spectral analyses;
- (b) multi-spectral glacier classification from ASTER data is compared to glacier mapping from other sensors, such as Ikonos (1 m) and Landsat (30 m);
- (c) the potential of repeated ASTER imagery for digital ice velocity measurements is evaluated;
- (d) combination of above techniques represents a powerful tool for assessing the potential of glacier-related hazards, as exemplified for glacier-lake outbursts.

Since the year 2000 imagery from ASTER has been available for global observation of land ice. ASTERs spectral and geometric capabilities include 3 bands in VNIR (visible and near infrared) with 15 m resolution, 6 bands in the SWIR (short-wave infrared) with 30 m, 5 bands in the TIR (thermal infrared) with 90 m (Fig. 1), and a 15 m resolution NIR along-track stereo-band looking 27.6° backwards from nadir (Fig. 2). The stereo band 3B covers the same spectral range of 0.76 μm - 0.86 μm as the nadir band 3N. The orbits of Terra and Landsat are the same, but ASTER swath width is 60 km, i.e. a third of the 180 km for Landsat. To image targets over the full swath width of Landsat, ASTER can be pointed ±8.5° cross-track between individual overflights (5, 6). Of special interest for glaciological studies are the high spatial resolution in VNIR, the stereo-, and the pointing-capabilities of ASTER.

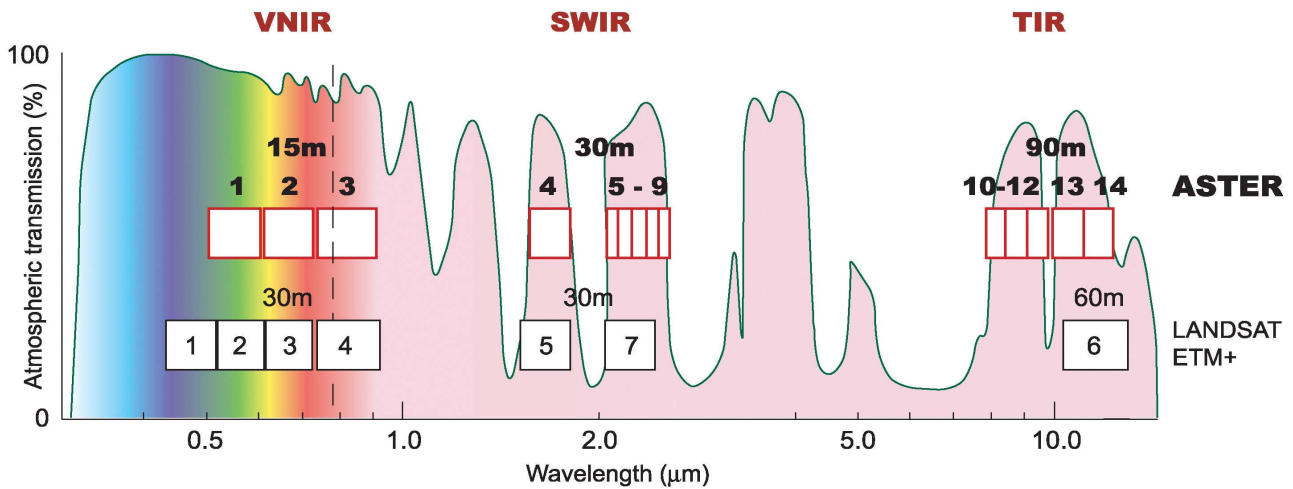


Figure 1: ASTER spectral bands (after 7), compared to Landsat ETM+. The rectangular boxes (red: ASTER, black: Landsat ETM+) indicate the sensor channels. The respective spatial resolution is indicated on top of the boxes. The coloured curve in the background represents the atmospheric transmission in dependency on the wavelength. The vertical dashed line marks the approximate margin of visible light. Abbreviations for sections of the light spectrum: VNIR (visible and near infrared), SWIR (short-wave infrared), and TIR (thermal infrared).

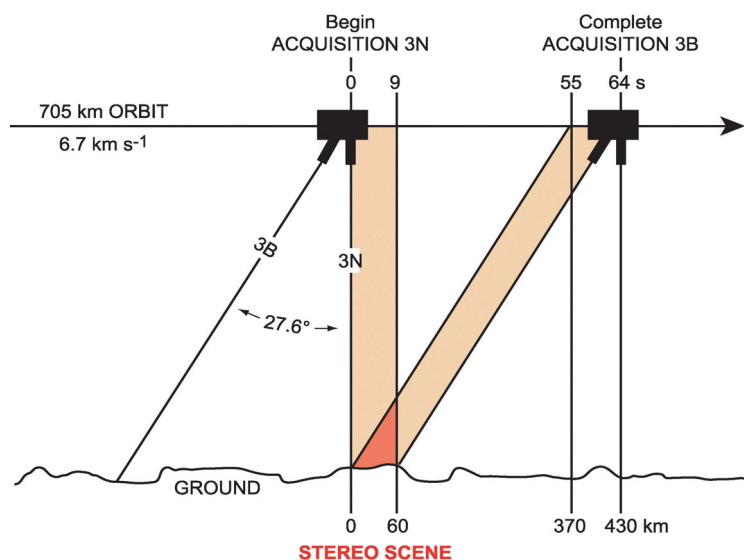


Figure 2: ASTER stereo geometry and timing of the nadir-band 3N and the back-looking sensor 3B (after 8). An ASTER nadir scene of approximately 60 km length, and a correspondent scene looking back by 27.6° off-nadir angle and acquired about 60 seconds later, form, together, a stereo scene.

Automatic DEM-Generation and Ortho-Projection

Deriving digital elevation models (DEM) from satellite stereo-imagery is not a new approach. Especially multi-temporal SPOT data from different pointing-angles have been widely used for DEM generation over mountainous terrain (1, 9, 10). A major problem, thereby, consists in the time lapse between the used images which – under high-mountain conditions – usually leads to different snow cover on the stereo images. These difficulties are overcome by along-track stereo-channels, such as available from ASTER.

For generating DEMs from ASTER data we either use level 1B corrected data, or level 1A data which are destriped using the respective parameters provided in the image header information. Orientation of the 3N and corresponding 3B band from ground control points (GCPs), transformation to epipolar geometry, parallax-matching, and parallax-to-DEM conversion is done using the software PCI Geomatica 8.0 Orthoengine (11). In areas with no sufficient ground control available we compute such information directly from the given satellite position and rotation angles. Thereby, the line-of-sight for an individual image point is intersected with the earth ellipsoid. The resulting position on the ellipsoid is corrected for the actual point elevation which, in turn, is estimated from the 3N-to-3B parallax of the selected GCP. Such GCPs are, then, imported into PCI Geomatica Orthoengine for computing the image orientation (so-called bundle adjustment). Fig. 3 shows an ASTER DEM (right) compared to a reference DEM (left) with 25 m grid-spacing derived directly from 1:30'000-scale aerial photography by analytical photogrammetry (12). The depicted test area Gruben in the Swiss Alps represents complex high-mountain conditions with high relief (1,800 m - 4,000 m a.s.l.), steep rock walls, deep cast shadows and snow fields without contrast. Therefore, we consider the test area to represent a worst-case scenario for DEM-generation from ASTER data.

Visual inspection and quantitative analysis show that severe errors of the ASTER DEM of up to approximately 500 m occur for sharp peaks with steep northern slopes which were completely missed (Fig. 3 and 4). These errors are not surprising considering the fact that such northern slopes are totally hidden in the back-looking band 3B, or are at least heavily distorted and, at the same time, lie in cast shadow. The overall vertical accuracy revealed by comparison of the ASTER DEM with the reference DEM amounts to ± 60 m RMS. For a subsection with smoother topography (rectangle in Figs. 3 and 4; elevation range 2,000 m – 2,900 m a.s.l.) an accuracy of ± 18 m RMS was found, i.e. approximately the ASTER VNIR pixel size of 15 m. Maximum errors within the subset of up to 95 m occur at sharp moraine ridges or deep stream channels. The elevation differences depicted in Fig. 4 indicate some systematic distortion with the ASTER DEM being too deep in the lower terrain parts, and too high in the upper terrain parts. This distortion could be successfully removed by introducing additional GCPs distributed over the entire altitudinal range. The above overall accuracy, however, was little affected by such measures.

Ortho-rectification of the ASTER image is computed from the obtained ASTER DEM, again within PCI Geomatica Orthoengine. For the maximum 8.5° across-track pointing, the above estimated maximum height error of 500 m translates to a horizontal displacement of approximately 70 m, and the above 60 m RMS error to 8 m displacement. For the more moderate terrain (rectangle in Figs. 3 and 4), the corresponding displacements are 14 m for 95 m elevation error or 2.5 m for 18 m RMS elevation error. In conclusion, for glacier surfaces which correspond roughly to the above moderate topography, a maximum positional error of one ASTER VNIR pixel of 15 m has to be expected in the orthoimages, depending on the cross-track pointing angle. (Remark: the ASTER VNIR, but not the SWIR and TIR sensors, can be pointed by $\pm 24^\circ$. We do not use imagery pointed by more than 8.5° because of the strong distortions, and because our terrain studies are usually combined with multi-spectral analysis applying also the SWIR and TIR bands.)

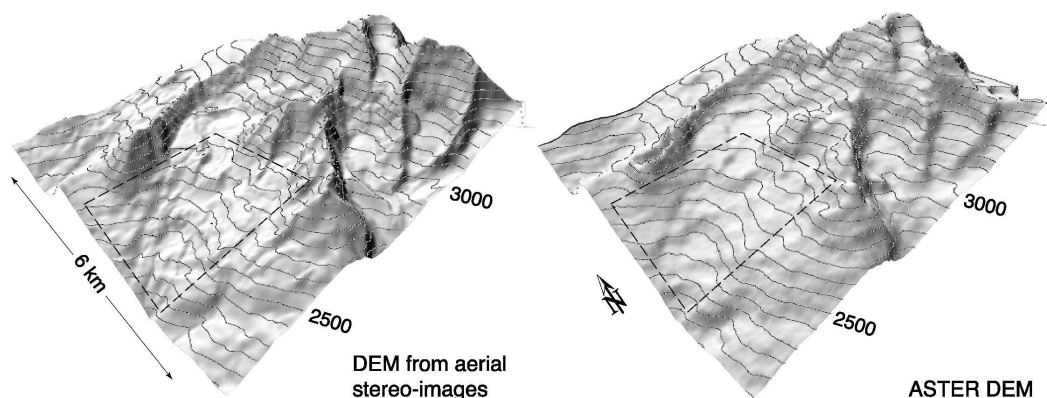


Figure 3: Gruben area, Swiss Alps: Perspective view of a shaded reference-DEM from aerial photogrammetry (left) compared to an automatic DEM from ASTER imagery (right). Black lines represent contour lines of 100m interval. The dashed rectangle indicates a subset with more moderate terrain (cf. Fig 4). The photogrammetric DEM was compiled based on 1:30'000-scale aerial imagery using an analytical plotter. The ASTER DEM was computed using the PCI Orthoengine software. In general, the agreement between the two DEMs appears to be good. The photogrammetric DEM shows more details as expected from the better image resolution. Gross errors occur at steep and high peaks (c.f. Fig 4).

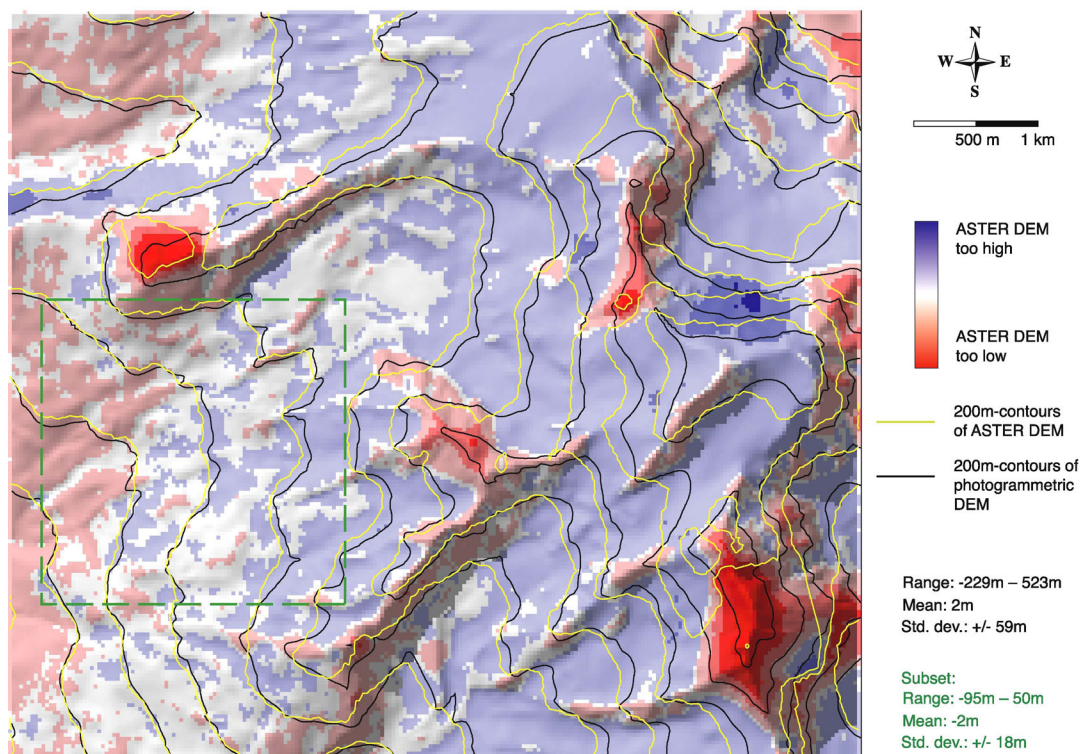


Figure 4: Colour-coded elevation differences between the aero-photogrammetric reference DEM and the ASTER DEM (c.f. Fig. 3), superimposed on a shaded relief of the photogrammetric DEM. Black lines: 200m-contours of the photogrammetric DEM; yellow lines: 200m-contours of the ASTER DEM. Largest errors (dark red and dark blue) of up to 500 m occur at sharp peaks, RMS error is ± 60 m. For a subset (green dashed rectangle; c.f. Fig 3) maximum errors of 95 m and a RMS error of ± 18 m were found. The general trend of a too high (= blue colours) ASTER DEM towards the higher terrain parts (left part of figure) points to some model distortion. Further tests showed that including more height control points does only partially reduce this effect.

GLACIER MAPPING

Various algorithms for automatically deriving glacier boundaries from multi-spectral imagery have been tested by (3, 13). The GLIMS initiative relies on a distributed system of regional centres and national stewards with local glaciological expertise. In order to allow related satellite-based glacier mapping to be performed also within less equipped processing centres, and to facilitate standardisation, we favour simple approaches such as band ratios for large-scale or even global applications such as GLIMS. Here, we mapped glacier outlines of the Susten / Furka region, Swiss Alps, from an ASTER image of 24 Aug 2001, and for comparison from a Landsat TM image of 12 Sep 1999 (Fig. 5). An algorithm by Paul (4, cf. also 14) was used which is based on glacier mapping from a thresholded TM 4/5 ratio image. For ASTER we used the equivalent bands 3 and 4 (cf. Fig. 1). To account for the different spatial resolution of ASTER bands 3 (15 m) and 4 (30 m), band 4 was re-sampled to 15 m resolution using bilinear interpolation.

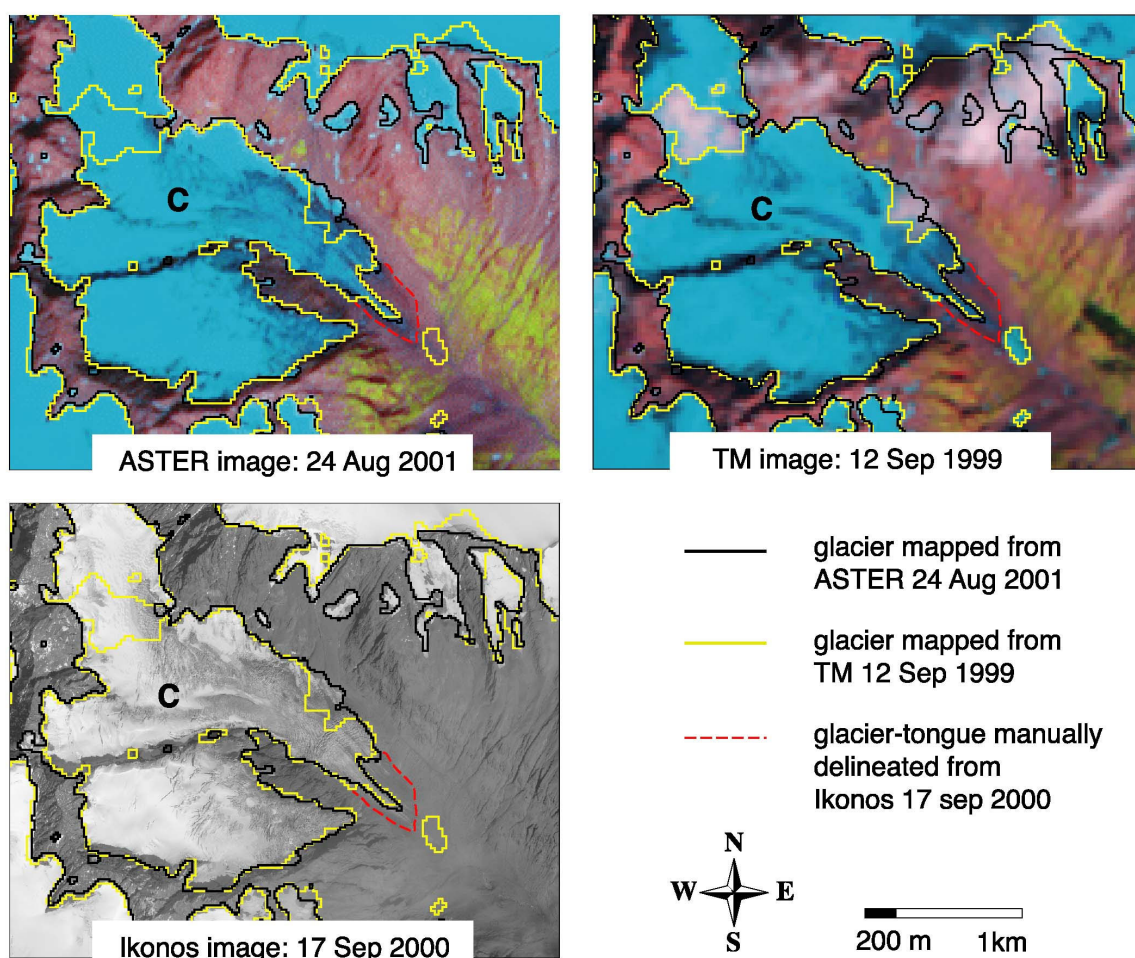


Figure 5: Glacier outlines in the Chelrenalp valley, Swiss Alps, as mapped automatically from an ASTER image of 24 Aug 2001 and a Landsat TM image of 12 Sep 1999. The debris-covered tongue of Chelrenalpgletscher (C) is manually delineated from an Ikonos image of 17 Sep 2000 (red dashed line). Upper left image: RGB-composite of ASTER 2 3 4, 15m resolution. Upper right image: RGB-composite of TM 3 4 5, 30m resolution. Lower left image: Ikonos panchromatic, 1m resolution. Yellow line: glacier outline automatically computed from a TM 4/5 ratio. Black line: glacier outline automatically computed from an ASTER 3/4 ratio. Largest differences between the TM and the ASTER glacier mapping are due to snow remains and clouds in 1999. Largest differences of the TM

and ASTER glacier mapping compared to the Ikonos image occur for debris-covered ice which is not detected from the multi-spectral ratios.

Visual inspection for the entire test area of roughly 50 km² suggests that the ASTER 3/4 glacier mapping might be slightly more reliable than the TM 4/5 mapping at some places (cf. Fig 5). As expected from the higher spatial resolution, ASTER 3/4 is able to follow small details more accurately than TM 4/5 (cf. 14). For most parts, however, both approaches show a good agreement to each other and to glaciers as visible on an Ikonos image of 17 Sep 2000. Both the applied band ratios for ASTER and TM are not able to map debris-covered ice as can be recognised at the tongue of Chelrenalpgletscher. Note that some severe errors in the 1999 glacier map from Landsat TM are due to small clouds.

Ice velocity measurements

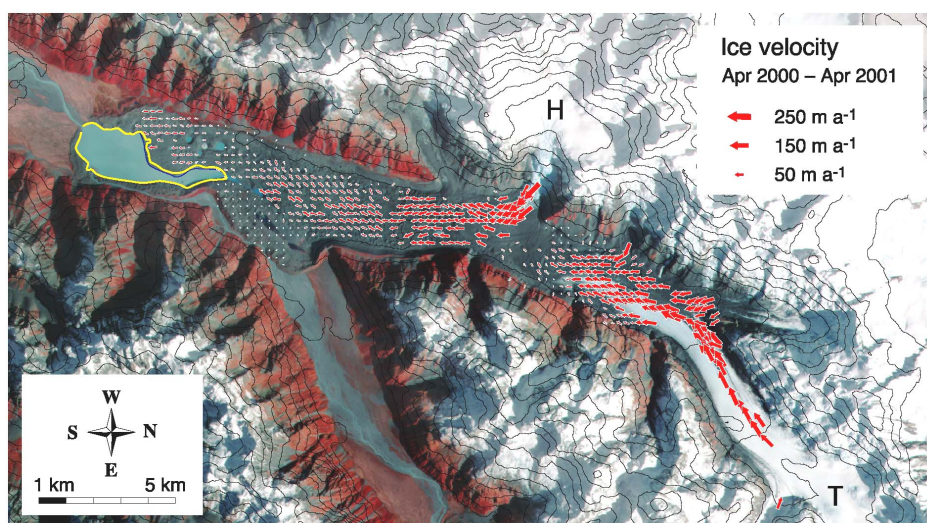
Concerning optical satellite data, horizontal displacements on glaciers have been measured mostly from repeated Landsat or SPOT data using different correlation techniques (15-20). For such work, the spatial resolution of the used images is the most crucial parameter, besides the time period between the acquisitions. Well-defined surface features, such as large crevasses or local debris cover, have to be identified at the available resolution. Here, multi-temporal orthoimages obtained from repeated ASTER imagery are used for measuring terrain displacements. The displacement of individual pixels or surface features between the multi-temporal satellite orthoimages is determined using a double cross-correlation technique (program CIAS, 21). Image interpolation beforehand the final image-matching reveals sub-pixel precision (i.e. a precision better than the 15 m pixel size). Using the georeference information of the orthoimages, the resulting displacement-parallaxes can be directly transformed into horizontal terrain displacements. In order to avoid distortions between the multi-temporal products, all imagery (i.e. 3N and 3B of time 1, and 3N and 3B of time 2) is bundle-adjusted as one image block connected by tie-points. For the multi-temporal connection of the stereo-models the tie-points have to be placed on stable terrain. (See (21) for details on the methodology.) Taking into account the fuzzy boundaries of most high-mountain terrain features at 15 m resolution, as well as considering terrain changes between the acquisition times, an overall accuracy of approximately one pixel size (i.e. 15 m) can be expected for the horizontal displacement measurements.

Figure 6 depicts the surface displacements between 2000 and 2001 for Tasman Glacier, New Zealand. The displacement vectors have been measured automatically from ASTER data of 29 April 2000 and 7 April 2001 using the software CIAS. The fact that one of the ASTER images was acquired in nadir mode, the other with 8.5° across-track pointing led to some low-frequency distortions within the orthoimages, presumably from errors in exterior orientation. In order to avoid these distortions affecting the displacement measurements, the glacier displacements were derived section-wise. For the individual image sections, planimetric orthoimage-to-orthoimage transformations were determined from apparently stable terrain points. The parameters of the section-wise transformations were applied to correct the raw displacement vectors. In Fig. 6 the original 100 m grid of measurements is resampled to a 200 m grid for better visibility. A threshold for individual correlation coefficients to be accepted was applied and few obvious miss-matches were deleted manually. Besides these procedures, Fig. 6 depicts the raw results. The automatic measurements did hardly succeed for clean or snow-covered ice, where the images showed no corresponding features for the two acquisitions. Especially for the upper glacier parts in April 2000, the ice was snow-covered.

In the upper part of Tasman Glacier, ice speeds of up to 230 m a⁻¹ were observed, continuously decreasing to the central part of the depicted image section where velocities are below the significance level of approximately one pixel (15 m). Thereby, the marked ice inflow with 250 m a⁻¹ (or even more) from the western tributary Hochstetter glacier might play an important role. Below this glacier confluence, velocities decrease again towards the lake at the glacier front. To the north-east of

the lake an area with very low or even zero velocities can be recognized, presumably consisting of ice-free moraine or stable dead-ice, de-coupled from the glacier.

The ice velocities measured from the ASTER data can be compared to some geodetic and aerophotogrammetric velocity measurements available for Tasman Glacier (22). For the lowermost 2 km – 3 km of the glacier terminus the velocities observed from ASTER data (approximately 15 m a^{-1} – 30 m a^{-1}) seem to be higher than those observed for 1971–86 (7 m a^{-1} – 11 m a^{-1}), and similar to those for 1957–71 (16 m a^{-1} – 24 m a^{-1}). Geodetic velocity measurements for May to December 1986 at a region 8 km upwards of the front gave 90 m a^{-1} . Velocities at the same place from ASTER data approximate 50 m a^{-1} for April 2000 to April 2001. Whilst the obtained velocity differences for the 2 km – 3 km section might not be significant considering the 15 m pixel size of ASTER, the variations for the 8 km section, however, indicate a marked difference in ice speed. It is not clear, whether this is, in fact, due to a general change in ice flow regime or just due to seasonal velocity



variations, since the terrestrial surveying of 1986 and the ASTER measurements cover different fractions of one year.

Figure 6: Ice flow vectors for Tasman Glacier, New Zealand, superimposed on an ASTER image of 29 April 2000. Contour lines of 200m interval are computed from the according ASTER DEM. The ice-flow vectors have been derived from automatic image correlation between ASTER images of 29 April 2000 and 7 April 2001. Ice speeds amount up to 250 m a^{-1} . The striking decrease of ice flow for Tasman Glacier (T) at the confluence with Hochstetter Glacier (H) indicates a complex interaction between both glaciers. At the glacier terminus the yellow line marks the lake extent of 7 April 2001 superimposed on the 29 April 2000 orthoimage. The observed lake growth towards the ice front amounts up to 130 m.

Close to the lake front, the ice velocities seem to slightly increase, potentially an effect of reduced friction at the glacier-bed by higher water pressure near the lake. During Apr 2000 – Apr 2001 the glacier front retreated by up to 130 m at the lake (Fig. 6). The measured flow field and retreat rates of Tasman Glacier are able to contribute to forecasting the evolution of the pro-glacial lake (23, 24). This lake evolution mainly consists in a balance of ice melt and break-off (calving), on the one hand, and ice supply from glacier flow, on the other hand.

Assessment of Glacier Hazard Potential

Glacier floods and related debris flows represent the most far-reaching glacier hazard, severely affecting human lives and infrastructure such as settlements, agricultural land, hydropower, and irrigation installations or transport networks. Glacier floods often originate from glacier or glacier-related lakes. Due to the – usually – remote location of such lakes remote sensing represents a pri-

mary tool for assessing and monitoring related outburst hazards. Lake detection is best done by multi-spectral analyses (25-27). Estimating the morphological characteristics of glacier lakes such as damming mechanism or erodible debris in the flood channel is greatly facilitated by combining spectral information with DEMs (26). Modelling of outburst floods and debris flows, finally, mandatory requires the availability of DEMs. Combining its high spatial and spectral resolution, and its



stereo ability for DEM generation, ASTER has the capability for integrated hazard-potential assessments using one sensor.

Figure 7: Simulation of the Dig Tsho outburst, Himalayas, based on an ASTER DEM. Dig Tsho is to the upper left of the image. Black lines indicate 100m-contour lines derived from the ASTER DEM. The erosion and deposition traces of a catastrophic flood in 1985 are still visible in the underlying ASTER image of 24 Apr 2001 as areas of destroyed vegetation coverage. In the RGB-composite of ASTER-channels 2 3 4, vegetation is indicated by red colours. The modelled flood path is depicted by a colour-transition from red over orange to yellow and green. The colours indicate high to low probabilities for a terrain point to be theoretically affected by any major runoff from the lake according to the applied model. In most parts, the modelled flood extent overlaps the actual flood traces, indicating that ASTER imagery and derived DEMs are useful for modelling potential glacier lake outburst floods. To the lower left of the image section clouds led to gross DEM errors.

Here, we reconstruct a lake outburst of Dig Tsho, Langmoche, Khumbu Himal, of 4 Aug 1985. The outburst flood of several 10^6 m^3 and the maximum runoff estimated to be $2,000 \text{ m}^3 \text{ s}^{-1}$ killed several people and destroyed a hydropower plant and many bridges (28). On an ASTER image of 24 Apr 2001 (Fig. 7) the erosion of this catastrophic outburst is still well visible. Using the 3N and 3B stereo bands of the respective scene a DEM was computed for the area. Based on this DEM and starting from the present lake extent a flood was simulated applying a single-flow GIS model (29). Whilst the model is not able to give any magnitude of the modelled flood, it shows the extent of the potentially affected areas and the corresponding hazard probability. Since these results are only dependent on the underlying DEM, a comparison of the actual flood path and the resulting erosion, respectively, with the modelled flood area provides a good estimate of the DEM and flood model quality. Despite of a zone of an obvious DEM error (center of Fig. 7) both the modelled and actual flood extents show good overlap. Gross DEM errors in the flood path as detected, for instance, by un-plausible model results or DEM reviewing, could be removed during DEM post-processing or editing.

Similar to lake outbursts, ice avalanche potentials can be modelled applying DEM-based avalanche models to steep glaciers which are, in turn, detected from multi-spectral classifications and DEM analyses (30). Glacier lakes or ice break-off hazards are often connected with glacier retreats or advances. These can be monitored from repeated satellite imagery (31, 32) and may be extrapolated using glacier parameterisation schemes (29, 33).

CONCLUSIONS

The presented case studies on DEM generation, glacier mapping, ice velocity measurements and glacier hazard assessment from ASTER data show that this sensor is highly suitable for worldwide glacier monitoring from space. Especially its combination of high spatial and spectral resolution and stereo capabilities enable applications which are to date difficult by other sensors. Geo-information systems (GIS) appear to be most suitable for integrating results from image processing and DEM analyses (31, 32). For suitable terrain conditions an ASTER DEM accuracy of one VNIR pixel of 15 m (RMS) can be expected with, however, marked problems for steep terrain. ASTER orthoimages computed from ASTER DEMs are less affected by such elevation errors, so that positional errors of usually less than 15 m result for the ortho-projection. Overlay of repeated ASTER orthoimages enables glacier velocity fields to be measured. As a rule of thumb, an accuracy for both ice velocities and elevation changes detected from repeated ASTER data of roughly one pixel (15 m RMS) may be expected.

However, some serious problems specific to high-mountain conditions (besides those specific to optical sensors in general) restrict the application of the presented methods for change detection: (i) Surface features with sufficient optical contrast must exceed the image resolution and have to be present over the observation period. These requirements are often difficult to fulfil in high mountains owing to ice and snow cover, ice and snow melt, frequent terrain destruction or convection clouds. (ii) The geometric changes might not exceed the significance level of the method applied. Therefore, glacier thickness changes, usually in the order of m a^{-1} can hardly be detected from repeated ASTER DEMs.

Potentially, two main image-acquisition parameters are available for meeting the above requirements: image resolution and time-base between the acquisitions. New and upcoming optical sensors are especially improving these parameters. (i) The increasing number of available sensors and imagery enhances the probability for finding suitable data. (ii) The number of (satellite-) sensors dedicated to customer-controlled acquisition increases, as (iii) also their spatial resolution does. In that context, ASTER is not only a valuable stand-alone tool for glacier monitoring but also a useful supplementary to other sensors. For large-scale glacier inventorying and monitoring the small ASTER swath width of 60 km is a clear disadvantage compared to Landsat ETM+ with 185 km. Automatic glacier mapping from Landsat TM (or ETM+) and ASTER multi-spectral imagery results, for most cases, in a comparable quality and accuracy.

Due to its limited spatial image-resolution and DEM accuracy the applicability of ASTER in the field of glacier hazards lies in the detection of hazard potentials rather than in detailed disaster forecast or process studies. For the former purpose, however, ASTER offers a number of possibilities, among which the combination of high spatial and spectral resolution and simultaneous DEMs might be the most prominent one.

ACKNOWLEDGEMENTS

The presented studies are partially financed by the Swiss National Science Foundation (21-54073.98, 21-59045.99). We are grateful to Sandra Eckert, Tobias Kellenberger, Klaus Seidel, and other colleagues who provided valuable support to the presented studies. Special thanks are due to Christian Mätzler for his comments on the manuscript.

REFERENCES

1. Kieffer, H.H. *et al.* 2000. New eyes in the sky measure glaciers and ice sheets. EOS Transactions, American Geophysical Union. 81(24): 265, 270-271.
2. Jacobs, J.D., Simms, E.L. and Simms, A. 1997. Recession of the southern part of Barnes Ice Cap, Baffin Island, Canada, between 1961 and 1993, determined from digital mapping of Landsat TM. Journal of Glaciology. 43: 98-102.
3. Sidjak, R.W. and Wheate, R.D. 1999. Glacier mapping of the Illecillewaet icefield, British Columbia, Canada, using Landsat TM and digital elevation data. International Journal of Remote Sensing. 20: 273-284.
4. Paul, F. 2002. Changes in glacier area in Tyrol, Austria, between 1969 and 1992 derived from Landsat 5 Thematic Mapper and Austrian Glacier Inventory data. International Journal of Remote Sensing. 23(4): 787-799.
5. ERSDAC. 1999. ASTER User's Guide. Part I(2). Earth Remote Sensing Data Analysis Center, Tokyo, Japan.
6. ERSDAC. 1999. ASTER User's Guide. Part II(2). Earth Remote Sensing Data Analysis Center, Tokyo, Japan.
7. NASA. NASA's Earth Observation System. ASTER brochure. (National Aeronautics and Space Administration, Japanese Ministry of International Trade and Industry, Jet Propulsion Laboratory, Goddard Space Flight Center, .
8. Lang, H.R. and Welch, R. 1999. Algorithm theoretical basis document for ASTER digital elevation models. Version 3.0. NASA's Earth Observation System.
9. Al-Rousan, N. and Petrie, G. 1998. System calibration, geometric accuracy testing and validation of DEM & orthoimage data extracted from SPOT stereopairs using commercially available image processing systems. International Archives of Photogrammetry & Remote Sensing. 34(4): 8-15.
10. Zomer, R., Ustin, S. and Ives, J. 2002. Using satellite remote sensing for DEM extraction in complex mountainous terrain: landscape analysis of the Makalu Barun National Park of eastern Nepal. International Journal of Remote Sensing. 23(1): 125-143.
11. Toutin, T. and Cheng, P. 2001. DEM generation with ASTER stereo data. Earth Observation Magazine. 10(6): 10-13.
12. Käab, A. 2001. Photogrammetric reconstruction of glacier mass balance using a kinematic ice-flow model: a 20-year time-series on Grubengletscher, Swiss Alps. Annals of Glaciology. 31: 45-52.
13. Paul, F. 2001. Evaluation of different methods for glacier mapping using Landsat TM. Proceedings EARSeL Workshop on Remote Sensing of Land Ice and Snow , 16.-17.6.2000, Dresden, 239-245.
14. Paul, F. *et al.* 2002. Comparison of TM-derived glacier areas with higher resolution data sets. Proceedings EARSeL Workshop on Remote Sensing of Land Ice and Snow, Bern, 11.-13.3.2002, .
15. Lucchitta, B.K. and Ferguson, H.M. 1986. Antarctica - measuring glacier velocity from satellite images. Science. 234(4780): 1105-1108.
16. Scambos, T.A. *et al.* 1992. Application of image cross-correlation to the measurement of glacier velocity using satellite image data. Remote Sensing of Environment. 42(3): 177-186.
17. Whillans, I.M., Jackson, M. and Tseng, Y.H. 1993. Velocity pattern in a transect across Ice Stream B, Antarctica. Journal of Glaciology. 39(133): 562-572.
18. Frezzotti, M., Capra, A. and Vittuari, L. 1998. Comparison between glacier ice velocities inferred from GPS and sequential satellite images. Annals of Glaciology. 27: 54-60.

19. Seko, K. *et al.* 1998. Changing surface features of Khumbu glacier, Nepal Himalayas revealed by SPOT images. *Bulletin of Glacier Research*. 16: 33-41.
20. Nakawo, M., Yabuki, H. and Sakai, A. 1999. Characteristics of Khumbu Glacier, Nepal Himalaya: recent change in the debris-covered area. *Annals of Glaciology*. 28: 118-122.
21. Kääb, A. and Vollmer, M. 2000. Surface geometry, thickness changes and flow fields on permafrost streams: automatic extraction by digital image analysis. *Permafrost and Periglacial Processes*. 11(4): 315-326.
22. Kirkbride, M. 1995. Ice flow vectors on the debris-mantled Tasman glacier, 1957-1986. *Geografiska Annaler*. 77 A(3): 147-157.
23. Kirkbride, M.P. and Warren, C.R. 1999. Tasman glacier, New Zealand: 20th-century thinning and predicted calving retreat. *Global and Planetary Change*. 22: 11-28.
24. Purdie, J. and Fitzharris, B. 1999. Processes and rates of ice loss at the terminus of Tasman glacier, New Zealand. *Global and Planetary Change*. 22: 79-91.
25. Kääb, A. *et al.* 2000. Glacier- and permafrost-related hazards in high mountains: Integrative assessment in the Swiss Alps based on remote sensing and geo-information systems. *Proceedings X Congresso Peruano de Geologia, Lima, CD-ROM*.
26. Huggel, C. *et al.* 2002. Remote sensing based assessment of hazards from glacier lake outbursts: a case study in the Swiss Alps. *Canadian Geotechnical Journal*. 39(2): 316-330.
27. Wessels, R., Kargel, J.S. and Kieffer, H.H. 2002. ASTER measurement of supraglacial lakes in the Mount Everest region of the Himalaya. *Annals of Glaciology*. 34, in press.
28. Vuichard, D. and Zimmermann, M. 1987. The 1985 catastrophic drainage of a moraine-dammed lake, Khumbu Himal, Nepal: causes and consequences. *Mountain Research and Development*. 7(2): 91-110.
29. Huggel, C. *et al.* 2002. Assessment of glacier hazards and glacier runoff for different climate scenarios based on remote sensing data: a case study for a hydropower plant in the Peruvian Andes. *Proceedings EARSeL workshop*, 11.-13.03.2002, Berne .
30. Salzmann, N. 2002. Modellierung von Gefahrenpotentialen durch Eislawinen mittels Fernerkundung und GIS. Department of Geography, University of Zurich. Diploma thesis.
31. Paul, F. *et al.* 2002. The new remote sensing derived Swiss glacier inventory: I. Methods. *Annals of Glaciology*. 34: 355-361.
32. Kääb, A. *et al.* 2002. The new remote sensing derived Swiss glacier inventory: II. First results. *Annals of Glaciology*. 34: 362-366.
33. Haeberli, W. and Hoelzle, M. 1995. Application of inventory data for estimating characteristics of and regional climate-change effects on mountain glaciers: a pilot study with the European Alps. *Annals of Glaciology*. 21: 206-212.